

Washington University School of Medicine

Digital Commons@Becker

2020-Current year OA Pubs

Open Access Publications

11-7-2022

High-throughput analysis of tissue microarrays using automated desorption electrospray ionization mass spectrometry

Nicolás M Morato
Purdue University

Hannah Marie Brown
Washington University School of Medicine in St. Louis

Diogo Garcia
Mayo Clinic

Erik H Middlebrooks
Mayo Clinic

Mark Jentoft
Mayo Clinic

See next page for additional authors

Follow this and additional works at: https://digitalcommons.wustl.edu/oa_4



Part of the [Medicine and Health Sciences Commons](#)

Recommended Citation

Morato, Nicolás M; Brown, Hannah Marie; Garcia, Diogo; Middlebrooks, Erik H; Jentoft, Mark; Chaichana, Kaisorn; Quiñones-Hinojosa, Alfredo; and Cooks, R Graham, "High-throughput analysis of tissue microarrays using automated desorption electrospray ionization mass spectrometry." *Scientific Reports*. 12, 1. 18851 (2022).

https://digitalcommons.wustl.edu/oa_4/847

This Open Access Publication is brought to you for free and open access by the Open Access Publications at Digital Commons@Becker. It has been accepted for inclusion in 2020-Current year OA Pubs by an authorized administrator of Digital Commons@Becker. For more information, please contact vanam@wustl.edu.

Authors

Nicolás M Morato, Hannah Marie Brown, Diogo Garcia, Erik H Middlebrooks, Mark Jentoft, Kaisorn Chaichana, Alfredo Quiñones-Hinojosa, and R Graham Cooks



OPEN

High-throughput analysis of tissue microarrays using automated desorption electrospray ionization mass spectrometry

Nicolás M. Morato^{1,6}, Hannah Marie Brown^{1,2,6}, Diogo Garcia³, Erik H. Middlebrooks^{3,4}, Mark Jentoft⁵, Kaisorn Chaichana³, Alfredo Quiñones-Hinojosa³ & R. Graham Cooks¹✉

Tissue microarrays (TMAs) are commonly used for the rapid analysis of large numbers of tissue samples, often in morphological assessments but increasingly in spectroscopic analysis, where specific molecular markers are targeted via immunostaining. Here we report the use of an automated high-throughput system based on desorption electrospray ionization (DESI) mass spectrometry (MS) for the rapid generation and online analysis of high-density (6144 samples/array) TMAs, at rates better than 1 sample/second. Direct open-air analysis of tissue samples (hundreds of nanograms) not subjected to prior preparation, plus the ability to provide molecular characterization by tandem mass spectrometry (MS/MS), make this experiment versatile and applicable to both targeted and untargeted analysis in a label-free manner. These capabilities are demonstrated in a proof-of-concept study of frozen brain tissue biopsies where we showcase (i) a targeted MS/MS application aimed at identification of isocitrate dehydrogenase mutation in glioma samples and (ii) an untargeted MS tissue type classification using lipid profiles and correlation with tumor cell percentage estimates from histopathology. The small sample sizes and large sample numbers accessible with this methodology make for a powerful analytical system that facilitates the identification of molecular markers for later use in intraoperative applications to guide precision surgeries and ultimately improve patient outcomes.

Tissue microarrays (TMAs) are widely utilized tools for high-throughput pathology and molecular biology^{1–6}. A TMA typically consists of hundreds of small tissue core samples, derived from many donor specimens, and embedded in a paraffin block^{1–11}. Sectioning of a TMA then yields multiple slides containing hundreds of tissue sections (0.6–3 mm in diameter) arranged in a grid pattern that allows simultaneous examination of many clinical samples under identical conditions^{1–6,9–11}. The use of TMAs has facilitated the rapid and efficient molecular profiling of tissue samples through parallel evaluation of one or several molecular markers at the protein, DNA, or RNA level, using techniques such as immunohistochemistry (IHC), fluorescence in situ hybridization, or mRNA in situ hybridization, respectively^{1,3,5–7,10,12}. Nowadays TMAs are utilized to screen different tissue types, assess the clinical significance of molecular alterations in cancer and other diseases, and to evaluate the effectiveness of novel pharmaceuticals^{12–24}. Such wide applications of TMAs follow from their clear advantages over individual tissue examination, which include decreased assay time and cost, experimental uniformity, and low sample utilization^{1,4,6,8–10}.

In contrast to antibody-based IHC and in situ hybridization screens, label-free methods for TMA analysis allow for untargeted exploratory studies or rapid evaluation of specific biomarkers without use of staining protocols, providing further flexibility for the use of TMAs in clinical research. For instance, Fourier transform infrared (FTIR) spectroscopic analysis of TMAs has been utilized for histopathologic recognition of prostate and breast cancer^{25–28}, oral squamous cell carcinoma²⁹, and even cellular and acellular tissue constituents^{28,30}, in most

¹Department of Chemistry, Purdue Center for Cancer Research, and Bindley Bioscience Center, Purdue University, 560 Oval Drive, West Lafayette, IN 47907, USA. ²Present address: Department of Pathology and Immunology, Washington University School of Medicine, St. Louis, MO, USA. ³Department of Neurosurgery, Mayo Clinic, Jacksonville, FL, USA. ⁴Department of Radiology, Mayo Clinic, Jacksonville, FL, USA. ⁵Department of Laboratory Medicine and Pathology, Mayo Clinic, Jacksonville, FL, USA. ⁶These authors contributed equally: Nicolás M. Morato and Hannah Marie Brown. ✉email: cooks@purdue.edu

cases relying on sophisticated machine learning algorithms for data analysis^{26,30}. Similar applications have been demonstrated using Raman spectroscopy^{31–34}. In the case of mass spectrometry (MS), characterization of TMAs has been mainly done using matrix-assisted laser desorption ionization (MALDI) and has been heavily focused on protein analysis^{35–38}. This approach has been successful at the characterization and subtyping of lung^{39,40} kidney⁴¹, and thyroid⁴² cancers, as well as the prediction of treatment response in breast cancer xenografts⁴³ and in head and neck cancer samples⁴⁴. Note that MALDI allows for the high-throughput analysis of TMAs, but it usually requires ionization in vacuum using a laser source and typically involves extensive sample preparation. Specifically for TMA analysis, widely reported MALDI protocols include TMA slide deparaffinization, heat-induced antigen retrieval, in situ enzymatic digestion, and matrix deposition steps before MS analysis^{35,37,38}.

In this work we propose a simple method for the rapid generation of high-density (up to 6144 samples per array) TMAs followed by direct (i.e. no sample workup) online analysis using desorption electrospray ionization (DESI) MS. DESI is an ambient ionization technique for direct analysis of complex samples, such as tissue, in the open air^{45–47}. It utilizes a charged solvent spray to impact the sample surface, desorb and ionize the molecules present, and carry them to the mass spectrometer for analysis⁴⁵. As spatial control of the sampling event is readily available, DESI-MS has been extensively utilized for imaging of many complex biological samples, including various tissue types where the small-molecule profiles obtained have allowed for differentiation between cancerous and non-cancerous tissue in a multitude of human organs, albeit in a low-throughput manner^{47–54}. Recently, high-throughput (> 1 sample per second) DESI-MS analysis has been successfully demonstrated for the screening of organic reactions^{55–63}, the development of label-free biological assays^{64,65}, and the generation of large spectral libraries^{66,67} using an automated platform that combines custom and commercial robotics, software, and MS instrumentation⁶⁸. Here we expand the capabilities of this high-throughput DESI-MS platform to the rapid creation and direct characterization of TMAs via their small-molecule profiles using frozen brain biopsies as a proof-of-concept study. We anticipate this high-throughput methodology to have applications in retrospective studies and in support of MS-based intraoperative diagnosis^{69–78}, the latter by aiding in the efficient identification of new biomarkers or the generation of robust classification models (both using large sample sets) which can then be translated to point-of-care applications in the operating room.

Methods

Samples. Two TMAs were analyzed in this study. The first TMA (TMA1) was composed of a collection of 36 frozen and unmodified human brain tissue biopsies purchased by Purdue University from the Biorepository of the Methodist Research Institute (Indianapolis, IN, USA). It is worth noting that this set of biopsies was acquired more than six years ago, sampled and analyzed on multiple occasions, and repeatedly freeze-thawed. However, it has an assortment of non-cancerous brain parenchyma samples, together with glioma, meningioma, and pituitary tumors, thus the choice to utilize it as part of this proof-of-concept study. The second TMA (TMA2) comprised 30 clinical human brain tissue biopsies from 9 patients undergoing tumor resection surgeries performed at Mayo Clinic (Jacksonville, FL, USA). The biopsies were taken from surgeon-defined positions within the tumor cavity with sampling positions being recorded by neuronavigational software. These biopsies were initially stored in the Biospecimen Accessioning and Processing Core at Mayo Clinic Florida and later sent to Purdue University for high-throughput DESI-MS analysis.

Histopathological and genetic analysis. All tissue biopsies were subjected to pathologic evaluation. For the banked tissue samples (TMA1), tissue biopsies were cryosectioned, mounted onto glass slides, and hematoxylin and eosin (H&E) stained. For the samples in TMA2, fresh tissue biopsies were smeared onto glass slides and H&E stained. Evaluation of disease state, tumor cell percentage (TCP), glioma subtype, and tumor grade of all tissue biopsies were made by senior neuropathologists (TMA2: M.J.). The IDH genotype of each subject was confirmed by IHC and/or genetic testing of a pathologic biopsy, methods consistent with standard of care. All the de-identified pathologic information is summarized in the Supporting Information (Supplementary Tables S1 and S2).

Generation and high-throughput DESI-MS(/MS) analysis of TMAs. High-density tissue microarrays (up to 6144 samples/array) were generated using a Beckman Biomek i7 fluid handling workstation (Beckman Coulter, Indianapolis, IN, USA) equipped with a 50-nL floating slotted 384-pin tool (V&P Scientific, San Diego, CA, USA). Brain biopsies were placed in individual wells of a 384-well microtiter plate (Greiner Bio-One, Monroe, NC, USA) which was then located on the deck of the workstation. Minimal amounts of tissue (< 500 ng) were sampled simultaneously from the microplate using the pin tool and spotted onto a DESI slide generating sample spots of ca. 800 μm diameter. DESI slides are prepared in house using custom soda-lime glass slides with the same footprint as a well plate (Abrisa Technologies, Santa Paula, CA, USA) and coated with a porous PTFE membrane (Zytek G-115; Saint-Gobain, Wayne, NJ) using a light film of low VOC spray adhesive (Scotch Spray Mount; 3 M, St. Paul, MN). Up to 6144 samples (equivalent to 16 individual 384-well plates) can be spotted on a single DESI plate with a center-to-center distance of ca. 1.1 mm at the highest density. The spotting step is fast, flexible (i.e. not all positions have to be utilized), and allows transfer of replicates from the same tissue sample, thus providing a more accurate average molecular profile of the tissue within the analysis of a single array. In this work, each biopsy was spotted four times, generating a 1536-position grid (note that all available positions were not completely utilized on any TMA). Importantly, as only ng amounts of sample are transferred, the source plate containing the almost intact tissue biopsies can be easily frozen and stored for further analyses in a virtually unperturbed state. Note that depending on the state of the tissue, the quality of the spotted sample might vary. In particular, we noticed occasional incomplete transfers from older and repeatedly freeze-thawed samples as well as from tissue showing a high degree of coagulation or necrosis.

After spotting, the slides are automatically transferred to a mass spectrometer equipped with a DESI stage and analyzed in a *spot-to-spot* manner after calibration of sample positions using three reference dye-marks near the corners of the plate. The effective analysis time (i.e. time spent on each sample) is ca. 500 ms in full scan mode and about 6 s for tandem MS (MS/MS) analysis, enough to obtain high-quality spectra regardless of the inherent variability across the spotted samples (as displayed in Supplementary Figure S1), likely from differences in transfer efficiency and amount of blood present. Both the data acquisition and DESI stage movement are automatically controlled using custom Python software⁵⁹. In this study, we chose to use two different mass spectrometers for TMA analysis. Full scan MS for untargeted molecular profiling of the tissue samples was carried out in the negative ion mode using a Synapt G2-Si quadrupole time-of-flight mass spectrometer equipped with a 2D DESI stage, a high-performance XS-generation DESI sprayer⁷⁹, and a heated transfer capillary (Waters, Milford, MA, USA). The DESI spray solvent flow rate was set to 1.5 $\mu\text{L}/\text{min}$ and the nebulizing nitrogen pressure was regulated to 20 psi. The heated transfer capillary was kept at 400 °C while the source temperature was set to 150 °C. Finally, the DESI spray voltage was selected as -0.75 kV and the scan time was fixed at 100 ms. MS/MS analysis was also performed in the negative ion mode using an LTQ XL linear ion trap (Thermo Scientific, Waltham, MA, USA) equipped with a DESI 2D stage (Prosolia, Zionsville, IN, USA). In this case the DESI spray solvent flow was set to 3 $\mu\text{L}/\text{min}$ and the nebulizing nitrogen pressure was fixed at 150 psi. The transfer capillary temperature was kept at 350 °C and the DESI spray voltage at -4.5 kV. Automated gain control was utilized with a maximum injection time of 500 ms. Methanol Chromasolv LC-MS grade (Honeywell Riedel-de Haën, Muskegon, MI, USA) was used as DESI solvent in all cases.

Full scan MS analysis was carried out for the untargeted molecular profiling of the tissue samples in order to assess the potential of the small-molecule profile to differentiate tissue types or correlate with estimated TCP values. On the other hand, MS/MS analysis was utilized for a targeted study aimed at the rapid determination of isocitrate dehydrogenase (IDH) mutation status of the brain cancer samples. This approach follows previous studies^{70,73,78} that have demonstrated the excellent classification performance of IDH-mutant and IDH-wildtype gliomas using the ratio between 2-hydroxyglutamic acid (2HG, m/z 147), an oncometabolite accumulated in IDH-mutant tissue, and glutamic acid (Glu, m/z 146), an endogenous compound whose concentration is typically reduced in IDH-mutant tumors^{80–84}. Thus, large 2HG:Glu ratios characterize IDH-mutant samples, whereas values close to zero are typical of IDH-wildtype tumors. To evaluate this ratio a single MS/MS experiment was utilized, simultaneously isolating both precursor ions using a window of m/z 3 units centered at m/z 146.5, then fragmenting both precursor ions simultaneously through collision-induced dissociation (CID; collision energy was set to 20 normalized manufacturer units), and evaluating their most intense transitions, i.e. m/z 147 \rightarrow m/z 129 for 2HG and m/z 146 \rightarrow m/z 128 for Glu. Note that the use of an ion ratio compensates for temporal variations in ion signal while the use of MS/MS provides higher specificity and reduced chemical noise.

The overall workflow is summarized in Fig. 1. Further details on hardware, software, and operation of the automated DESI-MS system have been described previously^{59,68}.

Data analysis. High-throughput DESI-MS full scan data for each array was acquired as a single RAW file whereas MS/MS spectra were recorded as one RAW file per each sample. In both cases, after acquisition was completed, RAW files were converted to mzXML format using MSConvert⁸⁵ and automatically processed using custom MATLAB (MathWorks, Natick, MA, USA) scripts. Briefly, MS spectral data was assigned to each individual spot using the DESI stage log (i.e. time, position), and further assigned to biopsy samples using the source plate layout input by the user (i.e. which biopsy was located in each well). To obtain equally spaced spectral vectors with common separation-unit values, individual scans were resampled and averaged across each spot. Average spot spectra were normalized to the base peak and then used to calculate average results per biopsy.

Average full scan mass spectra were initially subjected to principal component analysis (PCA) after standard normal variate (SNV) normalization. The estimated principal components were utilized as input features for supervised classification using the classification learner toolkit in MATLAB. Due to the small sample size, especially when considering individual class representation, models were trained using six-fold cross-validation. Several common robust machine learning algorithms were explored, namely bagged and boosted trees, as well as linear support vector machine. Optimized hyperparameters, identified using Bayesian optimization, as well as further model details are described in the Supporting Information (Supplementary Table S3). Significant compounds were tentatively assigned using exact mass measurements (mass error < 5 ppm), previous literature reports on MS profiling of brain samples^{54,71,86–91}, and the LIPID MAPS data base^{92,93}.

MS/MS spectra were readily assigned to biopsy samples using the source plate layout as sample position information is recorded within the file name of each MS/MS RAW file. Similarly, as only single spots on the array were used for MS/MS analysis, the scans in the file were automatically averaged to yield the results for each biopsy. The intensities of both 2HG and Glu were extracted from these averages as 1 m/z unit wide bins centered on the product ion signals at m/z 129 and m/z 128, respectively. Finally, the IDH mutation score was calculated for each biopsy using the extracted ion intensity information. This score is simply computed as the ratio of 2HG and Glu intensities with a correction for the ¹³C-Glu isotope product ion contribution to the 2HG signal, as shown in Eq. (1).

$$\text{IDH mutation score} = \frac{I_{129} - (I_{128} \times 6.1\%)}{I_{128}} \quad (1)$$

Ethical approval. Tumor and non-tumor tissue was obtained from patients undergoing craniotomies at Mayo Clinic Florida with approval of the Mayo Clinic Institutional Review Board (protocol 19-010725).

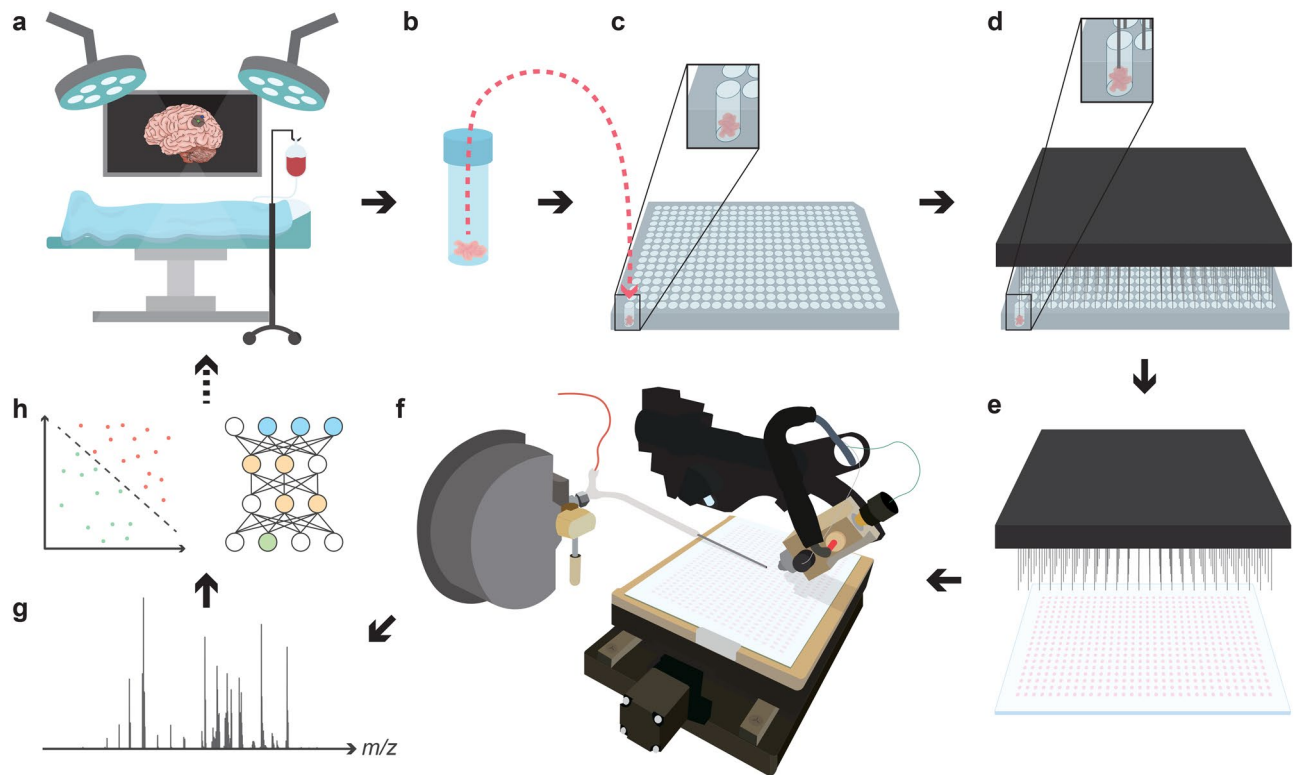


Figure 1. Overall workflow for the generation and high-throughput analysis of TMAs using automated DESI-MS. Biopsies are collected (a, b) and then arranged on a 384-well plate (c). Nanogram amounts of each biopsy are sampled using a pin-tool (d) and transferred to a DESI plate generating arrays with up to 6144 samples per plate (e). Both of these latter steps are carried out automatically using a fluid handling workstation. In this study, each biopsy was spotted four times to generate replicate samples in each TMA. Once ready, the plates are transferred to a DESI stage coupled to a mass spectrometer for analysis in a spot-to-spot fashion with throughputs better than 1 sample per second in full scan mode (f). Once the analysis is completed, spectra are automatically processed and assigned to the corresponding samples (g). Finally, the processed spectral data is utilized to identify/validate molecular markers or train classification methods (h) that can then be translated to MS-based intrasurgical applications.

Informed patient consent was obtained prior to collection. All methods were performed in accordance with relevant guidelines and regulations of the Institutional Review Board and the Declaration of Helsinki.

Results and discussion

IDH genotype assignment through targeted high-throughput DESI-MS/MS. Molecular markers underlie the diagnosis, prognosis, and potential treatment of gliomas^{94–96}. One such marker is associated with the mutation of the IDH enzyme, which plays a significant role in the accurate classification of gliomas and has prognostic value⁹⁷, as patients with IDH-mutant gliomas survive longer^{98,99} and can benefit from extensive resection^{100,101}. Mutation of this enzyme, whose wildtype function is the oxidative decarboxylation of isocitric acid to form α -ketoglutaric acid, leads to the accumulation of 2HG (Fig. 2a)^{102,103}, which can be readily measured intraoperatively by MS/MS using biopsy smears in ca. 3 min per sample^{70,73,78}. In laboratory settings, lower-throughput (ca. 30 min per sample) hyphenated chromatography-MS approaches have also been reported¹⁰⁴. Here we evaluate a targeted MS/MS approach for high-throughput (6 s per sample) IDH genotyping of glioma using TMAs.

The proposed MS/MS assessment relies on the simultaneous isolation and fragmentation of 2HG and Glu for calculation of an IDH mutation score. Despite the rapid analysis and low sample amounts, high quality signal is obtained, as observed in the representative MS/MS spectra corresponding to IDH-mutant and IDH-wildtype biopsies shown in Fig. 2b, c. While only tumor core biopsies are used for the assessment of IDH genotype intraoperatively due to tumor heterogeneity, we analyzed all samples on the TMAs and compared with the pathological information. Even so, perfect classification performance (100% accuracy within the sample set) is obtained for differentiation of IDH-mutant samples ($n_{\text{TMA1}} = 6$; $n_{\text{TMA2}} = 13$) from IDH-wildtype ($n_{\text{TMA1}} = 7$; $n_{\text{TMA2}} = 17$) or non-cancerous brain biopsies ($n_{\text{TMA1}} = 14$) for both TMAs (Fig. 2d). Such high accuracy of the DESI-MS/MS based IDH genotyping suggests the ability of this high-throughput method to validate molecular diagnostic approaches using large banked sample sets.

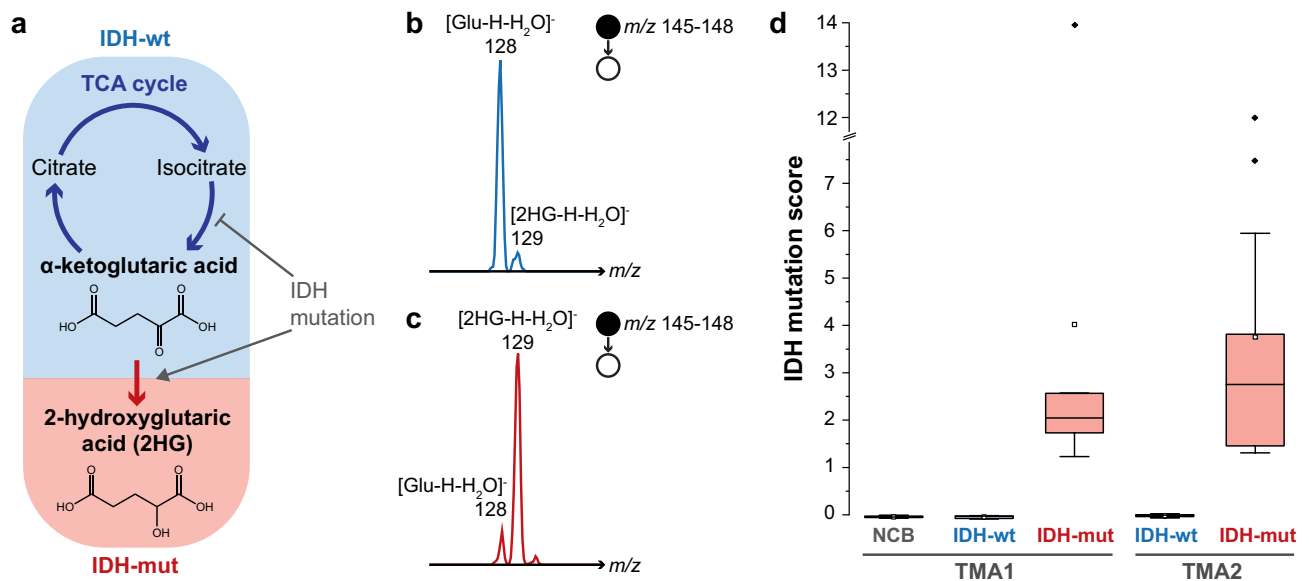


Figure 2. IDH genotype determination using high-throughput DESI-MS. In IDH-mutant (IDH-mut) gliomas, an alteration in the function of the IDH enzyme leads to the accumulation of 2HG (a), an oncometabolite that can be monitored easily by MS/MS in the negative ion mode. In a single MS/MS scan, using a 3 m/z unit window, both 2HG and Glu can be isolated and fragmented through CID allowing their $[M-H-H_2O]^-$ fragments to be monitored. Representative spectra for IDH-wildtype (IDH-wt; b) and IDH-mut (c) are both shown. Perfect classification of the samples in both TMAs (d) is achieved using the IDH mutation score (i.e. MS/MS ion ratio corrected for the ^{13}C -Glu isotopic contribution) calculated from 6 s of MS/MS acquisition per sample. In all cases boxes show the 25th–75th percentile with the median, while whiskers correspond to 1.5 interquartile range (IQR); averages and outliers (outside 1.5 IQR) as white and black symbols, respectively. NCB: non-cancerous brain samples.

Untargeted metabolic profiling with high-throughput DESI-MS. To assess the value of high-throughput DESI-MS for untargeted TMA metabolic profiling, we performed full MS analysis (1 s per sample) of both TMAs in the negative ion mode. In this case, the data from both arrays were analyzed separately as it has been demonstrated that the aging of biopsies, together with repeated freeze–thaw cycles¹⁰⁵, induce metabolic alterations that largely dominate the variability amongst samples even in the case of formalin-fixed paraffin-embedded specimens¹⁰⁶. PCA of all samples in TMA1 showed unsupervised clustering by tissue type in the three-dimensional space of the first two principal components (68% variance explained), with pituitary ($n=4$) and meningioma ($n=5$) tumors differing most from glioma ($n=13$) and from non-cancerous brain parenchyma ($n=14$) samples (Fig. 3a). These results are to be expected as the cells and tissues from which the different tumors arise are distinct (e.g. glia vs. meninges), and in agreement with previous studies^{54,107}. In fact, using the estimated principal components as input features ($m=35$), high accuracy (>90%; ROC AUCs ≥ 0.89) is obtained for supervised tissue classification using simple machine learning algorithms including bagged (Fig. 3b) and boosted trees, as well as support vector machine (Supplementary Table S3). In most cases, as expected from visual examination of the PCA results, misclassifications tend to occur only between non-cancerous brain parenchyma and glioma samples, particularly those that seem molecularly similar in the PCA space (Supplementary Figure S2). Interestingly, the glioma samples commonly misclassified as non-cancerous brain across the algorithms tested, correspond all to low-grade (WHO grade II) gliomas, which tend to be diffuse and are characterized by a low-proliferation index^{108,109}. This phenomenon clearly illustrates the complexity in classifying disease state in the presence of contributions by signals from both background parenchyma and tumor infiltration. Such tissue heterogeneity, especially near surgical margins, has been observed both intra- and post-operatively. Additional variability arising from glioma subtypes which might also affect classification performance has been previously reported^{86,110–112}. This effect could not be probed due to the small sample size ($n=13$ for all glioma samples; subtype class size: $1 \leq n \leq 5$), but we anticipate that it could be assessed using the HT DESI-MS methodology described here together with larger banked sets.

Unsupervised analysis of the results for TMA2, which contains only clinical glioma samples, agrees with previous reports on the correlation between the molecular profile of glioma biopsies and their estimated TCP^{54,69,78}, as it shows two main clusters in the two-dimensional PCA space (65% explained variance), one of low and low-moderate TCP samples and the other corresponding to biopsies identified with high and moderate-high TCP (Fig. 4a). Samples labeled as moderate TCP are found distributed across both clusters. Interestingly, the observed separation between the two groups is primarily captured by the first principal component (44% variance explained), making straightforward the identification of relevant features that characterize high TCP samples vs. low TCP ones through the calculated coefficients of this component (Fig. 4b; Supplementary Table S4) as well as the average mass spectra corresponding to each cluster (Supplementary Figure S3). Relevant compounds

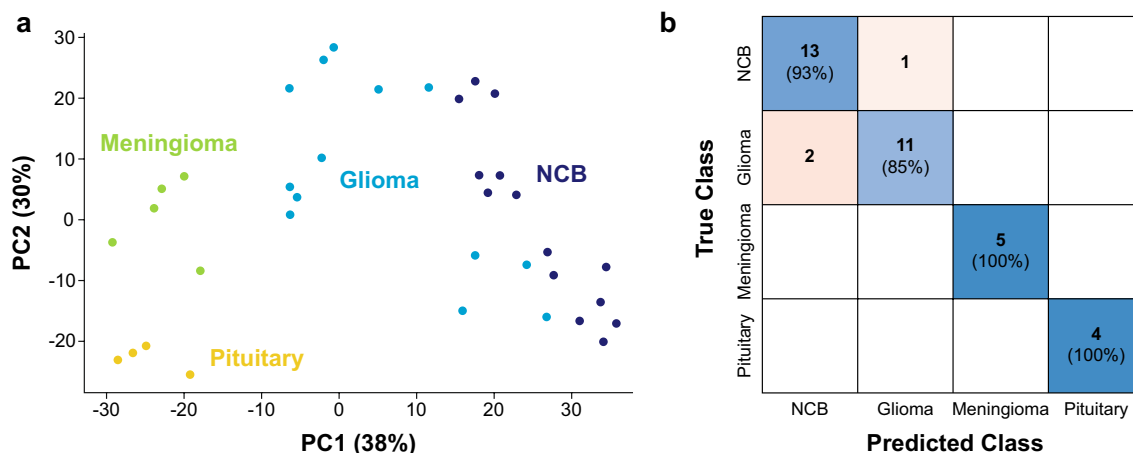


Figure 3. Untargeted analysis of TMA1 using full scan mass spectral data acquired in the negative ion mode. (a) Unsupervised clustering by tissue types was observed after PCA in the two-dimensional space generated with the first two principal components estimated (68% variance explained). Supervised classification of the samples using all the obtained principal components as features ($m = 35$) yielded overall 91.7% classification accuracy using a random forest model. (b) The model results are shown in the confusion matrix estimated via six-fold cross-validation. NCB: non-cancerous brain.

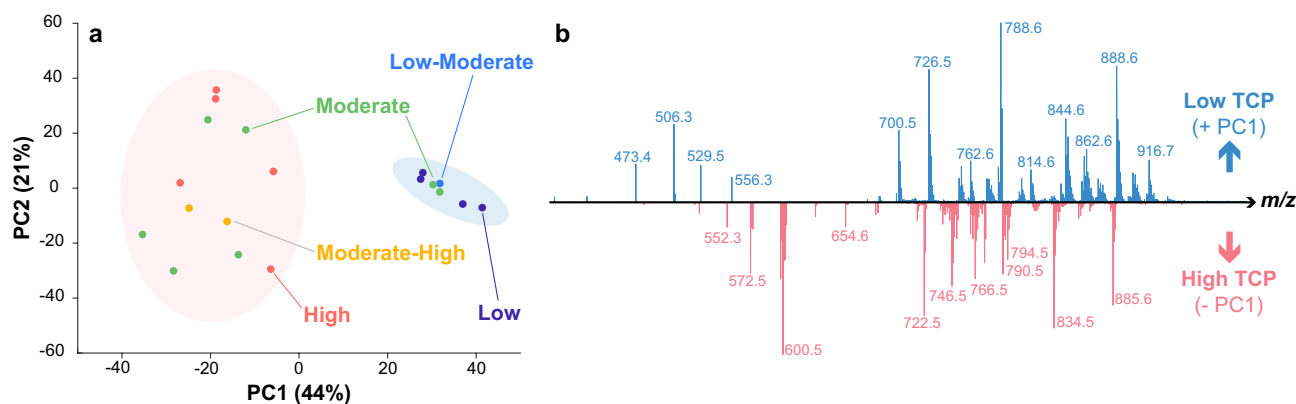


Figure 4. Untargeted analysis of TMA2 using full scan mass spectral data acquired in the negative ion mode. (a) Unsupervised clustering by estimated TCP was observed after PCA in the two-dimensional space generated with the first two principal components estimated (68% variance explained). (b) Observed separation between both groups is primarily associated with the first principal component (44% variance explained).

previously identified^{54,71} as markers of non-cancerous gray and white matter, including phosphatidylserine (PS) 36:1 (m/z 788.5) and the sulfatides (STs) 24:1 (m/z 888.6) and 24:1(OH) (m/z 904.6), were found clearly associated with lower TCP samples. Similarly, phosphatidylethanolamine (PE) 38:4 (m/z 766.5), phosphatidylcholine (PC) 34:1 ($[M + Cl]^-$; m/z 794.5), and phosphatidylinositol (PI) 38:4 (m/z 885.6), which have been previously identified with glioma tissue^{54,71}, are associated with higher TCP biopsies. PS 40:6 (m/z 834.5), formerly observed in both non-cancerous and glioma samples⁵⁴, was found more strongly associated with high TCP, as were PEs (40:6, m/z 790.5), plasmeyl-PEs (40:6, m/z 774.6; 38:4, m/z 750.5; 38:6, m/z 746.5; 36:4, m/z 722.5), and ceramides (40:2, m/z 654.6; 38:1, m/z 628.5; 36:1, m/z 600.5; 36:2, m/z 598.5; 34:1, m/z 572.5), these latter observed as $[M + Cl]^-$ adducts. Similarly, additional molecules suggestive of low TCP, included STs (26:1, m/z 916.7; 22:0, m/z 862.6; 22:1, m/z 860.6; 18:0, m/z 806.5) and plasmeyl-PEs (38:2, m/z 754.6; 36:2, m/z 726.5; 34:1, m/z 700.5).

The results obtained through this rapid untargeted profiling experiment indicate that HT DESI-MS has potential to efficiently generate and validate models of infiltrative margin determination, which is still a significant challenge during tumor resection^{100,111,113,114}. Such models hold high value as they could be directly translated to intraoperative MS diagnosis, an approach that has been increasingly demonstrated using both standard^{69–71,74–78} and miniature^{72,73,115} MS instrumentation, as well as MS coupled to robotic surgical systems⁷⁶.

Conclusions

DESI-MS is a common method for imaging of tissue sections and has been widely utilized to characterize multiple disease states in many tissue types. However, imaging typically requires long analysis times that are not compatible with high-throughput evaluation of large sample sets, such as TMAs. Here we demonstrate a novel

application of an automated high-throughput DESI-MS platform to generate and directly analyze high-density TMAs from frozen, unmodified tissue biopsies. Using a robotic fluid-handling workstation equipped with a pin tool we can create TMAs with up to 6144 samples per array using sub-microgram amounts of tissue. These TMAs are then automatically analyzed using DESI-MS with throughputs better than 1 sample per second for full scan MS screening and at rates close to 6 s per sample for MS/MS analysis. We demonstrated this new approach using brain cancer samples, showing that despite the low sample usage and the short analysis time, the spectral data obtained is of high quality and in agreement with previously reported results. In particular, we were able to assess IDH genotypes with 100% accuracy using a targeted MS/MS approach, clearly differentiating IDH-mutant from IDH-wildtype or non-cancerous brain parenchyma samples in two TMAs. We also explored the potential of using MS spectra as molecular profiles of the biopsies to differentiate tissue type (non-cancerous parenchyma, glioma, meningioma, pituitary) or to correlate with estimated TCP. Considering its minimal sample preparation, small volume of sample required, and high throughput, automated high-throughput DESI-MS also has potential value for the generation of spectral libraries for sample classification, the identification of biomarkers through large-scale studies, and the testing for biochemical activity or drug distributions in tissue.

Data availability

The raw datasets generated during and analyzed during the current study are available from the corresponding author on reasonable request.

Received: 15 August 2022; Accepted: 20 October 2022

Published online: 07 November 2022

References

- Oyejide, L., Mendes, O. R. & Mikaelian, I. Molecular Pathology: Applications in Nonclinical Drug Development in *A Comprehensive Guide to Toxicology in Nonclinical Drug Development* (ed. Faqi, A. S.) 407–445 (Academic Press, 2017).
- Battifora, H. The multitumor (sausage) tissue block: Novel method for immunohistochemical antibody testing. *Lab. Investig.* **55**, 244–248 (1986).
- Simon, R. & Sauter, G. Tissue microarrays for miniaturized high-throughput molecular profiling of tumors. *Exp. Hematol.* **30**, 1365–1372 (2002).
- Jawhar, N. M. T. Tissue Microarray: A rapidly evolving diagnostic and research tool. *Ann. Saudi Med.* **29**, 123 (2009).
- Le Page, C., Mes-Masson, A. M. & Magliocco, A. M. Tissue Microarrays in Studying Gynecological Cancers in *Cancer Genomics: From Bench to Personalized Medicine* (eds. Dellaire, G., Berman, J., Arceci R.) 65–76 (Academic Press, 2014).
- Kallioniemi, O. P., Wagner, U., Kononen, J. & Sauter, G. Tissue microarray technology for high-throughput molecular profiling of cancer. *Hum. Mol. Genet.* **10**, 657–662 (2001).
- Kononen, J. *et al.* Tissue microarrays for high-throughput molecular profiling of tumor specimens. *Nat. Med.* **4**, 844–847 (1998).
- Jensen, T. A. Advanced techniques. *J. Histotechnol.* **26**, 101–104 (2003).
- Jensen, T. A. & Hammond, M. E. The tissue microarray—A technical guide for histologists. *J. Histotechnol.* **24**, 283–287 (2001).
- Peerwani, Z. Tissue Microarrays in *Cell and Tissue Based Molecular Pathology* (eds. Tubbs, R. R. & Stoler, M. H.) 91–103 (Churchill Livingstone, 2009).
- Koo, M., Squires, J. M., Ying, D. & Huang, J. Making a tissue microarray. *Methods Mol. Biol.* **1897**, 313–323 (2019).
- Uhlén, M. *et al.* Tissue-based map of the human proteome. *Science* **347**, 6220, 1260419 (2015).
- Sipayya, V., Sharma, I., Sharma, K. C. & Singh, A. Immunohistochemical expression of IDH1 in gliomas: A tissue microarray-based approach. *J. Cancer Res. Ther.* **8**, 598 (2012).
- Xie, W. *et al.* Alterations of Smad signaling in human breast carcinoma are associated with poor outcome: A tissue microarray study. *Cancer Res.* **62**, 497–505 (2002).
- Torhorst, J. *et al.* Tissue microarrays for rapid linking of molecular changes to clinical endpoints. *Am. J. Pathol.* **159**, 2249–2256 (2001).
- Hierck, B. P., Iperen, L. V. Gittenberger-De Groot, A. C. & Poelmann, R. E. Modified indirect immunodetection allows study of murine tissue with mouse monoclonal antibodies. *Journal of Histochemistry & Cytochemistry* **42**, 1499–1502 (1994).
- Hoos, A. *et al.* Tissue microarray molecular profiling of early, node-negative adenocarcinoma of the rectum: A comprehensive analysis. *Clin. Cancer Res.* **8**, 3841–3849 (2002).
- Martinez-Morilla, S. *et al.* Quantitative assessment of PD-L1 as an analyte in immunohistochemistry diagnostic assays using a standardized cell line tissue microarray. *Lab. Invest.* **100**, 4–15 (2020).
- Al-Thawadi, H. *et al.* Co-presence of human papillomaviruses and Epstein-Barr virus is linked with advanced tumor stage: A tissue microarray study in head and neck cancer patients. *Cancer Cell Int.* **20**, 1–13 (2020).
- Steurer, S. *et al.* p63 expression in human tumors and normal tissues: a tissue microarray study on 10,200 tumors. *Biomark. Res.* **9**, 1–14 (2021).
- Coati, I. *et al.* Claudin-18 expression in oesophagogastric adenocarcinomas: A tissue microarray study of 523 molecularly profiled cases. *Br. J. Cancer* **121**, 257–263 (2019).
- Menz, A. *et al.* Diagnostic and prognostic impact of cytokeratin 19 expression analysis in human tumors: A tissue microarray study of 13,172 tumors. *Hum. Pathol.* **115**, 19–36 (2021).
- Fredholm, H. *et al.* Long-term outcome in young women with breast cancer: A population-based study. *Breast Cancer Res. Treat.* **160**, 131–143 (2016).
- Gremel, G. *et al.* A systematic search strategy identifies cubilin as independent prognostic marker for renal cell carcinoma. *BMC Cancer* **17**, 1–9 (2017).
- Lazaro-Pacheco, D. *et al.* Deciphering the structural and chemical composition of breast cancer using FTIR spectroscopy. *Appl. Spectrosc. Rev.* **57**, 234–248 (2022).
- Bhargava, R., Fernandez, D. C., Hewitt, S. M. & Levin, I. W. High throughput assessment of cells and tissues: Bayesian classification of spectral metrics from infrared vibrational spectroscopic imaging data. *Biochimica et Biophysica Acta BBA Biomembr.* **1758**, 830–845 (2006).
- Kumar, S., Desmedt, C., Larsimont, D., Sotiriou, C. & Goormaghtigh, E. Change in the microenvironment of breast cancer studied by FTIR imaging. *Analyst* **138**, 4058 (2013).
- Fernandez, D. C., Bhargava, R., Hewitt, S. M. & Levin, I. W. Infrared spectroscopic imaging for histopathologic recognition. *Nat. Biotechnol.* **23**, 469–474 (2005).
- Ellis, B. G. *et al.* Insight into metastatic oral cancer tissue from novel analyses using FTIR spectroscopy and aperture IR-SNOM. *Analyst* **146**, 4895–4904 (2021).

30. Berisha, S. *et al.* Deep learning for FTIR histology: leveraging spatial and spectral features with convolutional neural networks. *Analyst* **144**, 1642–1653 (2019).
31. Lazaro-Pacheco, D., Shaaban, A. M., Titiloye, N. A., Rehman, S. & Rehman, I. U. Elucidating the chemical and structural composition of breast cancer using Raman micro-spectroscopy. *EXCLI J.* **20**, 1118 (2021).
32. Bhamidipati, M., Lee, G., Kim, I. & Fabris, L. SERS-based quantification of PSMA in tissue microarrays allows effective stratification of patients with prostate cancer. *ACS Omega* **3**, 16784–16794 (2018).
33. Grosset, A. A. *et al.* Identification of intraductal carcinoma of the prostate on tissue specimens using Raman micro-spectroscopy: A diagnostic accuracy case–control study with multicohort validation. *PLoS Med.* **17**, e1003281 (2020).
34. Honda, K. *et al.* On-tissue polysulfide visualization by surface-enhanced Raman spectroscopy benefits patients with ovarian cancer to predict post-operative chemosensitivity. *Redox Biol.* **41**, 66 (2021).
35. Groseclose, M. R., Massion, P. P., Chaurand, P. & Caprioli, R. M. High-throughput proteomic analysis of formalin-fixed paraffin-embedded tissue microarrays using MALDI imaging mass spectrometry. *Proteomics* **8**, 3715–3724 (2008).
36. Aichler, M. & Walch, A. MALDI imaging mass spectrometry: Current frontiers and perspectives in pathology research and practice. *Lab. Invest.* **95**, 422–431 (2015).
37. Casadonte, R., Longuespée, R., Kriegsmann, J. & Kriegsmann, M. MALDI IMS and cancer tissue microarrays. *Adv. Cancer Res.* **134**, 173–200 (2017).
38. Casadonte, R. & Caprioli, R. M. Proteomic analysis of formalin-fixed paraffin-embedded tissue by MALDI imaging mass spectrometry. *Nat. Protoc.* **6**, 1695–1709 (2011).
39. Kriegsmann, M. *et al.* Mass spectrometry imaging for reliable and fast classification of non-small cell lung cancer subtypes. *Cancers* **12**, 2704 (2020).
40. Angel, P. M. *et al.* Extracellular matrix alterations in low-grade lung adenocarcinoma compared with normal lung tissue by imaging mass spectrometry. *J. Mass Spectrom.* **55**, e4450 (2020).
41. Drake, R. R. *et al.* Defining the human kidney N-glycome in normal and cancer tissues using MALDI imaging mass spectrometry. *J. Mass Spectrom.* **55**, e4490 (2020).
42. Kurczyk, A. *et al.* Classification of thyroid tumors based on mass spectrometry imaging of tissue microarrays: A single-pixel approach. *Int. J. Mol. Sci.* **21**, 6289 (2020).
43. Mascini, N. E. *et al.* The use of mass spectrometry imaging to predict treatment response of patient-derived xenograft models of triple-negative breast cancer. *J. Proteome Res.* **14**, 1069–1075 (2015).
44. Mascini, N. E., Teunissen, J., Noorlag, R., Willems, S. M. & Heeren, R. M. A. Tumor classification with MALDI-MSI data of tissue microarrays: A case study. *Methods* **151**, 21–27 (2018).
45. Takáts, Z., Wiseman, J. M., Gologan, B. & Cooks, R. G. Mass spectrometry sampling under ambient conditions with desorption electrospray ionization. *Science* **306**, 471–473 (2004).
46. Cooks, R. G., Ouyang, Z., Takats, Z. & Wiseman, J. M. Ambient mass spectrometry. *Science* **311**, 1566–1570 (2006).
47. Wiseman, J. M. *et al.* Desorption electrospray ionization mass spectrometry: Imaging drugs and metabolites in tissues. *Proc. Natl. Acad. Sci.* **105**, 18120–18125 (2008).
48. Eberlin, L. S. *et al.* Cholesterol sulfate imaging in human prostate cancer tissue by desorption electrospray ionization mass spectrometry. *Anal. Chem.* **82**, 3430–3434 (2010).
49. Inglese, P., Correia, G., Pruski, P., Glen, R. C. & Takats, Z. Colocalization features for classification of tumors using desorption electrospray ionization mass spectrometry imaging. *Anal. Chem.* **91**(10), 6530–6540 (2019).
50. Banerjee, S. *et al.* Diagnosis of prostate cancer by desorption electrospray ionization mass spectrometric imaging of small metabolites and lipids. *Proc. Natl. Acad. Sci.* **114**, 3334–3339 (2017).
51. Margulis, K. *et al.* Combining desorption electrospray ionization mass spectrometry imaging and machine learning for molecular recognition of myocardial infarction. *Anal. Chem.* **90**, 12198–12206 (2018).
52. Yan, X. *et al.* Cell-type-specific metabolic profiling achieved by combining desorption electrospray ionization mass spectrometry imaging and immunofluorescence staining. *Anal. Chem.* **92**, 13281–13289 (2020).
53. Bensussan, A. V. *et al.* Distinguishing non-small cell lung cancer subtypes in fine needle aspiration biopsies by desorption electrospray ionization mass spectrometry imaging. *Clin. Chem.* **66**, 1424–1433 (2020).
54. Jarmusch, A. K. *et al.* Lipid and metabolite profiles of human brain tumors by desorption electrospray ionization-MS. *Proc. Natl. Acad. Sci.* **113**, 1486–1491 (2016).
55. Wlekinski, M. *et al.* High throughput reaction screening using desorption electrospray ionization mass spectrometry. *Chem. Sci.* **9**, 1647–1653 (2018).
56. Jaman, Z., Mufti, A., Sah, S., Avramova, L. & Thompson, D. H. High throughput experimentation and continuous flow validation of Suzuki–Miyaura cross-coupling reactions. *Chem. Eur. J.* **24**, 9546–9554 (2018).
57. Jaman, Z. *et al.* Rapid on-demand synthesis of lomustine under continuous flow conditions. *Org. Process Res. Dev.* **23**, 334–341 (2019).
58. Jaman, Z. *et al.* High-throughput experimentation and continuous flow evaluation of nucleophilic aromatic substitution reactions. *ACS Comb. Sci.* **22**, 184–196 (2020).
59. Sobreira, T. J. P. *et al.* High-throughput screening of organic reactions in microdroplets using desorption electrospray ionization mass spectrometry (DESI-MS): Hardware and software implementation. *Anal. Methods* **12**, 3654–3669 (2020).
60. Ewan, H. S. *et al.* Aldol reactions of biorenewable triacetic acid lactone precursor evaluated using desorption electrospray ionization mass spectrometry high-throughput experimentation and validated by continuous flow synthesis. *ACS Comb. Sci.* **22**, 796–803 (2020).
61. Biyani, S. A. *et al.* Use of high-throughput tools for telescoped continuous flow synthesis of an alkynyl naphthyridine anticancer agent, HSN608. *Org. Process Res. Dev.* **24**, 2240–2251 (2020).
62. Logsdon, D. L. *et al.* High-throughput screening of reductive amination reactions using desorption electrospray ionization mass spectrometry. *Org. Process Res. Dev.* **24**, 1647–1657 (2020).
63. Huang, K.-H., Ghosh, J., Xu, S. & Cooks, R. G. Late-stage functionalization and characterization of drugs by high-throughput desorption electrospray ionization mass spectrometry. *ChemPlusChem* **87**, 1, e202100449 (2021).
64. Morato, N. M., Holden, D. T. & Cooks, R. G. High-throughput label-free enzymatic assays using desorption electrospray ionization mass spectrometry. *Angew. Chem. Int. Ed.* **59**, 20459–20464 (2020).
65. Kulathunga, S. C., Morato, N. M., Zhou, Q., Cooks, R. G. & Mesecar, A. D. Desorption electrospray ionization mass spectrometry assay for label-free characterization of SULT2B1b enzyme kinetics. *ChemMedChem* **17**, 9 e202200043 (2022).
66. Qiu, L., Morato, N. M., Huang, K. & Cooks, R. G. Spontaneous water radical cation oxidation at double bonds in microdroplets. *Front. Chem.* **10**, 903774 (2022).
67. Le, M. T., Morato, N. M., Kaerner, A., Welch, C. J. & Cooks, R. G. Fragmentation of polyfunctional compounds recorded using automated high-throughput desorption electrospray ionization. *J. Am. Soc. Mass Spectrom.* **32**, 2261–2273 (2021).
68. Morato, N. M., Le, M. T., Holden, D. T. & Graham Cooks, R. Automated high-throughput system combining small-scale synthesis with bioassays and reaction screening. *SLAS Technol.* **26**, 555–571 (2021).
69. Pirro, V. *et al.* Intraoperative assessment of tumor margins during glioma resection by desorption electrospray ionization-mass spectrometry. *Proc. Natl. Acad. Sci.* **114**, 201706459 (2017).

70. Alfaro, C. M. *et al.* Intraoperative assessment of isocitrate dehydrogenase mutation status in human gliomas using desorption electrospray ionization–mass spectrometry. *J. Neurosurg.* **4**(132), 180–187 (2019).
71. Pirro, V. *et al.* Analysis of human gliomas by swab touch spray-mass spectrometry: Applications to intraoperative assessment of surgical margins and presence of oncometabolites. *Analyst* **142**, 4058–4066 (2017).
72. Pu, F. *et al.* Rapid determination of isocitrate dehydrogenase mutation status of human gliomas by extraction nanoelectrospray using a miniature mass spectrometer. *Anal. Bioanal. Chem.* **411**, 1503–1508 (2019).
73. Brown, H. M. *et al.* Intraoperative detection of isocitrate dehydrogenase mutations in human gliomas using a miniature mass spectrometer. *Anal. Bioanal. Chem.* **411**, 7929–7933 (2019).
74. Sans, M. *et al.* Performance of the MasSpec pen for rapid diagnosis of Ovarian cancer. *Clin. Chem.* **65**, 674–683 (2019).
75. Brown, H. M., Pirro, V. & Cooks, R. G. From DESI to the MasSpec pen: Ambient ionization mass spectrometry for tissue analysis and intrasurgical cancer diagnosis. *Clin. Chem.* **64**, 628–630 (2018).
76. Keating, M. F. *et al.* Integrating the MasSpec Pen to the da Vinci surgical system for in vivo tissue analysis during a robotic assisted porcine surgery. *Anal. Chem.* **92**, 11535–11542 (2020).
77. King, M. E. *et al.* Rapid diagnosis and tumor margin assessment during pancreatic cancer surgery with the MasSpec Pen technology. *Proc. Natl. Acad. Sci.* **118**, 66 (2021).
78. Brown, H. M. *et al.* Intraoperative mass spectrometry platform for IDH mutation status prediction, glioma diagnosis, and estimation of tumor cell infiltration. *J. Appl. Lab. Med.* **6**, 902–916 (2021).
79. Morato, N. M. & Cooks, R. G. Inter-platform assessment of performance of high-throughput desorption electrospray ionization mass spectrometry. *Talanta Open* **4**, 100046 (2021).
80. Nagashima, H. *et al.* Diagnostic value of glutamate with 2-hydroxyglutarate in magnetic resonance spectroscopy for IDH1 mutant glioma. *Neuro Oncol.* **18**(11), 1559–1568 (2016).
81. Ruiz-Rodado, V. *et al.* Metabolic plasticity of IDH1-mutant glioma cell lines is responsible for low sensitivity to glutaminase inhibition. *Cancer Metab.* **8**, 23 (2020).
82. Han, S. *et al.* IDH mutation in glioma: Molecular mechanisms and potential therapeutic targets. *Br. J. Cancer* **122**, 1580–1589 (2020).
83. Chen, R., Brown, H. M. & Cooks, R. G. Metabolic profiles of human brain parenchyma and glioma for rapid tissue diagnosis by targeted desorption electrospray ionization mass spectrometry. *Anal. Bioanal. Chem.* **413**, 6213–6224 (2021).
84. McBrayer, S. K. *et al.* Transaminase inhibition by 2-hydroxyglutarate impairs glutamate biosynthesis and redox homeostasis in glioma. *Cell* **175**, 101–116.e25 (2018).
85. Chambers, M. C. *et al.* A cross-platform toolkit for mass spectrometry and proteomics. *Nat. Biotechnol.* **30**, 918–920 (2012).
86. Eberlin, L. S. *et al.* Classifying human brain tumors by lipid imaging with mass spectrometry. *Can. Res.* **72**, 645–654 (2012).
87. Otsuka, Y. *et al.* Imaging mass spectrometry of a mouse brain by tapping-mode scanning probe electrospray ionization. *Analyst* **139**, 2336–2341 (2014).
88. Guan, X. L. *et al.* Non-targeted profiling of lipids during kainate-induced neuronal injury. *FASEB J.* **20**, 1152–1161 (2006).
89. Fincher, J. A. *et al.* Matrix-free mass spectrometry imaging of mouse brain tissue sections on silicon nanopost arrays. *J. Comp. Neurol.* **527**, 2101–2121 (2019).
90. Blomqvist, M. *et al.* High-throughput analysis of sulfatides in cerebrospinal fluid using automated extraction and UPLC-MS/MS. *J. Lipid Res.* **58**, 1482–1489 (2017).
91. Paine, M. R. L. *et al.* Three-dimensional mass spectrometry imaging identifies lipid markers of medulloblastoma metastasis. *Sci. Rep.* **9**, 2205 (2019).
92. Sud, M. *et al.* LMSD: LIPID MAPS structure database. *Nucleic Acids Res.* **35**, D527–D532 (2007).
93. Fahy, E., Sud, M., Cotter, D. & Subramaniam, S. LIPID MAPS online tools for lipid research. *Nucleic Acids Res.* **35**, W606–W612 (2007).
94. Eckel-Passow, J. E. *et al.* Glioma groups based on 1p/19q, IDH, and TERT promoter mutations in tumors. *N. Engl. J. Med.* **372**, 2499–2508 (2015).
95. Killock, D. CNS cancer: Molecular classification of glioma. *Nat. Rev. Clin. Oncol.* **12**, 502 (2015).
96. Ellison, D. W. Multiple molecular data sets and the classification of adult diffuse gliomas. *N. Engl. J. Med.* **372**, 2555–2557 (2015).
97. Darvishi, P. *et al.* Prognostic value of preoperative MRI metrics for diffuse lower-grade glioma molecular subtypes. *Am. J. Neuroradiol.* **41**, 815–821 (2020).
98. Brat, D. J. *et al.* cIMPACT-NOW update 5: Recommended grading criteria and terminologies for IDH-mutant astrocytomas. *Acta Neuropathol.* **139**, 603–608 (2020).
99. Aoki, K. *et al.* Prognostic relevance of genetic alterations in diffuse lower-grade gliomas. *Neuro Oncol.* **20**, 66–77 (2018).
100. Choi, J. *et al.* Extent of resection and molecular pathologic subtype are potent prognostic factors of adult WHO grade II glioma. *Sci. Rep.* **10**, 1–8 (2020).
101. Beiko, J. *et al.* IDH1 mutant malignant astrocytomas are more amenable to surgical resection and have a survival benefit associated with maximal surgical resection. *Neuro Oncol.* **16**, 81–91 (2014).
102. Waitkus, M. S., Diplas, B. H. & Yan, H. Biological role and therapeutic potential of IDH mutations in cancer. *Cancer Cell* **34**, 186–195 (2018).
103. Dang, L. *et al.* Cancer-associated IDH1 mutations produce 2-hydroxyglutarate. *Nature* **462**, 739–744 (2009).
104. Xu, H. *et al.* Rapid diagnosis of IDH1-mutated gliomas by 2-HG detection with gas chromatography mass spectrometry. *Lab. Invest.* **99**, 588–598 (2018).
105. Boustany, N. N., Crawford, J. M., Manoharan, R., Dasari, R. R. & Feld, M. S. Effects of freeze-thaw and photobleaching on the ultraviolet resonance Raman spectra of human colon biopsies. *Appl. Spectrosc.* **55**, 1506–1513 (2001).
106. Ogrinc, N. *et al.* Direct water-assisted laser desorption/ionization mass spectrometry lipidomic analysis and classification of formalin-fixed paraffin-embedded sarcoma tissues without dewaxing. *Clin. Chem.* **67**, 1513–1523 (2021).
107. Calligaris, D. *et al.* Molecular typing of meningiomas by desorption electrospray ionization mass spectrometry imaging for surgical decision-making. *Int. J. Mass Spectrom.* **377**, 690–698 (2015).
108. Forst, D. A., Nahed, B. V., Loeffler, J. S. & Batchelor, T. T. Low-Grade Gliomas. *Oncologist* **19**, 403–413 (2014).
109. Brown, T. J. *et al.* Management of low-grade glioma: A systematic review and meta-analysis. *Neuro-Oncol. Pract.* **6**, 249–258 (2019).
110. Eberlin, L. S. *et al.* Ambient mass spectrometry for the intraoperative molecular diagnosis of human brain tumors. *Proc. Natl. Acad. Sci.* **110**, 1611–1616 (2013).
111. van Hese, L. *et al.* Towards real-time intraoperative tissue interrogation for REIMS-guided glioma surgery. *J. Mass Spectrom.* *Adv. Clin. Lab* **24**, 80–89 (2022).
112. Eberlin, L. S. *et al.* Discrimination of human astrocytoma subtypes by lipid analysis using desorption electrospray ionization imaging mass spectrometry. *Angew. Chem. Int. Ed.* **49**, 5953–5956 (2010).
113. Pekmezci, M. *et al.* Detection of glioma infiltration at the tumor margin using quantitative stimulated Raman scattering histology. *Sci. Rep.* **11**, 12162 (2021).
114. Nie, S. *et al.* Clinicopathologic analysis of microscopic tumor extension in glioma for external beam radiotherapy planning. *BMC Med.* **19**, 269 (2021).
115. Zou, R. *et al.* Point-of-care tissue analysis using miniature mass spectrometer. *Anal. Chem.* **91**, 1157–1163 (2019).

Acknowledgements

The authors thank neuropathologist Dr. Eyas Hattab for providing expert readings of the biospecimens in TMA1 and Rong Chen for her contributions during the collection of the TMA2 specimens. This work was supported by the Innovative Molecular Analysis Technologies (IMAT) Program of the National Cancer Institute of the National Institutes of Health (R33CA240181-01A1) and Waters Corporation (grant 40002775). A.Q.-H. acknowledges the support from Richard and Lauralee Uihlein, the William J. and Charles H. Mayo Professorship, the Mayo Clinic Clinician Investigator Award, the Florida Department of Health Cancer Research Chair Fund, and the Monica Flynn Jacoby Endowed Chair. N.M.M. acknowledges support from the American Chemical Society Division of Analytical Chemistry Graduate Fellowship sponsored by Agilent Technologies.

Author contributions

N.M.M. and H.M.B. contributed equally. R.G.C., N.M.M. and H.M.B. conceptualized the study. N.M.M. and H.M.B. collected and analyzed the data. D.G., E.M., K.C., and A.Q.-H. collected the TMA2 samples. M.J. provided histopathological analysis of the TMA2 samples. N.M.M., H.M.B. and R.G.C. wrote the manuscript. All authors read, critically revised, and approved the final manuscript. R.G.C., A.Q.-H., and K.C. acquired funding.

Competing interests

The authors declare no competing interests.

Additional information

Supplementary Information The online version contains supplementary material available at <https://doi.org/10.1038/s41598-022-22924-4>.

Correspondence and requests for materials should be addressed to R.G.C.

Reprints and permissions information is available at www.nature.com/reprints.

Publisher's note Springer Nature remains neutral with regard to jurisdictional claims in published maps and institutional affiliations.



Open Access This article is licensed under a Creative Commons Attribution 4.0 International License, which permits use, sharing, adaptation, distribution and reproduction in any medium or format, as long as you give appropriate credit to the original author(s) and the source, provide a link to the Creative Commons licence, and indicate if changes were made. The images or other third party material in this article are included in the article's Creative Commons licence, unless indicated otherwise in a credit line to the material. If material is not included in the article's Creative Commons licence and your intended use is not permitted by statutory regulation or exceeds the permitted use, you will need to obtain permission directly from the copyright holder. To view a copy of this licence, visit <http://creativecommons.org/licenses/by/4.0/>.

© The Author(s) 2022